U.S. Department of CommerceNational Oceanic and Atmospheric AdministrationNational Weather Service National Centers for Environmental Prediction 5200 Auth Road Camp Springs, MD 20746

Office Note 464

Revision of Convection and Vertical Diffusion Schemes in the NCEP Global Forecast System

Jongil Han[1] and Hua-Lu Pan[2]

[1]Wyle Information Systems LLC.
Environmental Prediction Center
National Centers for Environmental Predictions
Camp Springs, MD 20746

[2] Environmental Prediction Center
National Centers for Environmental Predictions
Camp Springs, MD 20746

Corresponding author address: 5200 Auth Rd., Camp Springs, MD, 20746

E-mail: jongil.han@noaa.gov

Abstract

A new physics package containing revised convection and planetary boundary layer (PBL) schemes in the National Centers for Environmental Prediction's Global Forecast System is described. The shallow convection (SC) scheme in the revision employs a mass flux parameterization replacing the operational turbulent diffusion based approach. For the deep convection scheme, the random cloud top selection in the current operational scheme is replaced by an entrainment rate parameterization with the rate dependent upon environmental moisture. The effects of the convection-induced pressure gradient force on cumulus momentum transport and convective overshooting are parameterized in both deep and shallow convection schemes and a modification of the trigger function has been developed. In addition, the PBL model is revised to enhance turbulence diffusion in stratocumulus regions.

A remarkable difference between the new and operational SC schemes is seen in their heating behavior in lower atmospheric layers above the PBL. While the operational SC scheme using the diffusion approach produces a pair of layers with cooling above and heating below in lower atmospheric layers, the new SC scheme using the mass-flux approach produces heating throughout the convection layers due to the dominant environmental subsidence warming. In particular, the new SC scheme helps to form stratocumulus clouds in the regions off the West coasts of South America and Africa, whereas the old scheme destroys them. Significant improvements in the forecasts of the global 500 hPa height, vector wind, and precipitation over the continental US are found with the revised model. In particular, unrealistic forecasts of excessive heavy precipitation have been significantly reduced due to the revision of the convection

schemes. Along with a reduction in vector wind forecast errors, hurricane track forecasts are considerably improved with the revised model, for both 2008 Atlantic and East Pacific hurricanes. Hurricane intensity forecasts are also significantly improved mainly due to the reduced momentum mixing in the revision.

1. Introduction

Toward improvement of the forecast performance, model physics in the National Centers for Environmental Prediction's (NCEP) Global Forecast System (GFS) model, the operational medium-range forecast model in the NCEP, is under continual development. However, few significant changes to the convection and vertical diffusion schemes have been made since 2001, due to the difficulty of satisfying the concomitant requirement for a careful consideration of interactions among model physics packages. In this paper, we present revised shallow and deep convection and vertical diffusion schemes based on advanced physical parameterizations, and evaluate the schemes for implementation in the operational NCEP GFS model.

The biggest change has been made in the shallow convection (SC) scheme. The current operational SC scheme in the NCEP GFS uses a simple turbulent eddy diffusion approach with a specified eddy diffusivity profile for the transport of sensible heat and moisture within convectively unstable layers, following the procedure proposed by Tiedtke et al. (1988). While this scheme has been successful in removing unrealistic moisture accumulation in the layer below the inversion by means of the additional diffusion of heat and moisture, it has suffered from the systematic underestimation of low clouds especially over near-shore regions in the eastern Pacific and Atlantic Oceans (Fig. 1). To better represent the physical processes of shallow convection, in this study we develop a bulk mass-flux parameterization. While the new SC scheme is based on the simplified Arakawa-Schubert (SAS) convection scheme (Pan and Wu, 1995) now used operationally in the NCEP GFS model for deep cumulus convection, many aspects in the

SAS scheme such as cloud base mass flux, entrainment and detrainment specifications, must be modified to accommodate the SC.

The deep convection scheme is also significantly modified here to suppress the unrealistic grid point storms, which are believed to result from the convective parameterization not fully eliminating the instability and consequently, causing explicit convective ascent to occur on the grid scale. Additionally, the effect of the convection-induced pressure gradient force on cumulus momentum transport (Han and Pan, 2005) is included in both shallow and deep convection parameterizations. Finally, the convection trigger function is modified and a parameterization for convective overshooting is developed, increasing cloud top.

The nonlocal planetary boundary layer (PBL) scheme in the NCEP GFS [so called MRF (Medium-range Forecast model) PBL model] proposed by Troen and Mahrt (1986) and implemented by Hong and Pan (1996) has been widely used for vertical diffusion because it provides not only a realistic development of a well-mixed layer despite its simplicity, but has also produced a consistent improvement in the skill of precipitation forecasts over the continental United States (Caplan et al., 1997). However, this scheme is optimized for simulation of dry boundary layers. To increase vertical diffusion in the cloudy region of the lower troposphere, therefore, a stratocumulus cloud top driven vertical diffusion scheme (Lock et al., 2000) is incorporated into the MRF PBL model along with the new SC scheme.

Details of these revisions are described below in section 2. In section 3, we evaluate the impact of the model physics changes. Finally, in section 4 we summarize our results and draw some conclusions.

2. Description of model physics changes

2. 1 Convection

a) Shallow convection

A turbulent eddy diffusion approach proposed by Tiedtke et al. (1988) is used for the SC in the current GFS. The scheme first looks for a convectively unstable layer, defined as the layer between the lifting condensation level (LCL) and the first neutral level above the LCL (but no higher than about the 700 hPa level), as a parcel originating in the second model layer is lifted. Then, vertical mixing of the heat and moisture within the convectively unstable layer is simulated with a parabolic eddy diffusivity profile with maximum value of 5 m^2s^{-1}. This diffusion approach for the SC may not be physically reasonable. For example, a mass-flux analogy for the vertical local turbulent diffusion (i.e., zero vertical velocity skewness; de Roode et al., 2000) indicates that the vertical turbulent transport can be represented by an updraft and downdraft with each occupying half the area in a given model grid box. For cumulus convection, on the other hand, the mass-flux approach assumes near-zero fractional area for the updraft in a given grid box, a more realistic assumption for the SC. With the mass-flux approach, therefore, the cloud environment is dominated by subsidence, resulting in environmental warming and drying, whereas the environmental change in the case of the eddy diffusion approach depends on vertical profile shapes of the environmental variables.

Since the mass-flux parameterization of SC developed in this study is based on the SAS deep convection scheme that can be found in Pan and Wu (1995), here we present only relevant equations that distinguish between the shallow and deep convection

schemes. As in the SAS scheme, a simple cloud model for the SC is used to describe the mass, moist static energy, and moisture within the updraft:

$$\frac{1}{\eta}\frac{\partial \eta}{\partial z} = \varepsilon - \delta \tag{1}$$

$$\frac{\partial(\eta s)}{\partial z} = (\varepsilon \bar{s} - \delta s)\eta \tag{2}$$

$$\frac{\partial[\eta(q_v + q_l)]}{\partial z} = \eta[\varepsilon \bar{q}_v - \delta(q_v + q_l) - r] \tag{3}$$

where η represents the mass flux normalized by the mass flux at the cloud base, ε the entrainment rate, δ the detrainment rate, s the moist static energy, q_v and q_l the vapor and liquid water mixing ratio in the updraft, r the precipitation, and the overbar the horizontal average. For the SC, it is assumed that there exist no convective scale downdrafts.

Vertical integration of Eqs. (1)-(3) requires the knowledge of cloud base mass flux and mass entrainment and detrainment. Cloud-base mass flux m_b is given as a function of the surface buoyancy flux (Grant, 2001), that is,

$$m_b = 0.03 w_* \tag{4}$$

where w_* is the convective velocity scale defined by

$$w_* = \left[(g/T_0)(\overline{w'\theta_v'})_0 h\right]^{1/3} \tag{5}$$

where h is the PBL height, g gravity, T_0 the reference temperature, and $(\overline{w'\theta_v'})_0$ the surface virtual kinematic heat flux. This differs from the SAS deep convection scheme, which uses a quasi-equilibrium closure of Arakawa and Schubert (1974) where the destabilization of an air column by the large-scale atmosphere is nearly balanced by the stabilization due to the cumulus.

While the convection starting level (CSL) in deep convection is defined as the level of maximum moist static energy between the surface and 700 hPa level from the surface, in SC it is assumed to be the level of maximum moist static energy within the PBL. The level of free convection (LFC) is used as the cloud base when a parcel is taken upward. Cloud top is initially assumed as the first neutral level encountered as the parcel is further lifted from the cloud base. A cloud thickness criterion distinguishes shallow from deep convection. Deep convection is checked first: if the cloud is thicker than 150 hPa, deep convection is activated; otherwise the convection is treated as shallow. Cloud top in the SC is limited to P/P_s=0.7 (where P is the layer pressure and the subscript s represents the ground surface). As described later in section 2.1c, the cloud top is increased for both deep and shallow convections by convective overshooting.

Large eddy simulation (LES) studies by Siebesma and Cuijpers (1995) indicate that the fractional entrainment and detrainment rates for the SC are one order of magnitude larger than values used in most of existing deep convection schemes. The LES study by Siebesma et al. (2003) indicates that a typical value for the fractional entrainment rate is $\varepsilon \sim 2.0\times10^{-3}$ near cloud base, in agreement with other LES studies (Siebesma and Cuijpers,1995; Grant and Brown, 1999) and observations (Raga et al., 1990), and that the entrainment rate behaves as

$$\varepsilon = c_e \frac{1}{z} \qquad (6)$$

where the empirical coefficient c_e =1.0. In this study, Eq. (6) with smaller value of c_e =0.3 is used for the SC entrainment rate. The detrainment rate is assumed to be a constant and given as the entrainment rate at the cloud base. In this way, the mass flux decreases with height above the cloud base, while it increases with height below the cloud base,

consistent with the abovementioned LES studies. The liquid water in the updraft layer is allowed to be detrained from every layer into the convective rain and grid-scale cloud water with conversion parameters of 0.002 m^{-1} and 5.0×10^{-4} m^{-1}, respectively.

The feedback of the cumulus convection onto the large-scale environment is accomplished via the compensating subsidence in the environment, the entrainment and detrainment processes between the cloud and environment. Although we allow precipitation processes for the SC, the initial tests indicate that precipitation by the SC is quite small.

b) Deep convection

Significant changes have also been made in the SAS deep convection scheme. As mentioned in the introduction, the current deep convection scheme does not appear to fully eliminate the instability and consequently, an explicit convective ascent occurs on the grid scale, producing unrealistically large precipitation. Random cloud top selection in the current SAS scheme is not used any longer, since it tends to make the cloud top lower on average and appears to weaken convection strength. To increase the convection strength further, the maximum allowable cloud base mass flux [M_{bmax}: currently 0.1 kg/(m^2s)] is increased by defining a local Courant-Friedrichs-Lewy (CFL) criterion to be satisfied (Jacob and Siebesman, 2003), i.e.,

$$M_{b\max} = \frac{\Delta p}{g\Delta t} \qquad (7)$$

where Δp and Δt are the depth of the model layer at cloud base and the model time step, respectively, and g the gravity. An initial test indicates that the M_{bmax} from Eq. (7) can be about 5 times larger than that in the current SAS scheme with T382 horizontal resolution (triangular truncation at wavenumber 382; about 35 km at the equator).

Unlike the current SAS, finite entrainment and detrainment rates for heat, moisture, and momentum are specified above cloud base. Following Bechtold et al. (2008), the entrainment is specified as

$$\varepsilon = \varepsilon_0 F_0 + d_1 (1 - RH) F_1 \tag{8}$$

$$F_0 = \left(\frac{\bar{q}_s}{\bar{q}_{sb}} \right)^2, \quad F_1 = \left(\frac{\bar{q}_s}{\bar{q}_{sb}} \right)^3$$

where ε_0 is the entrainment rate at the cloud base, RH the environmental relative humidity, d_1 a tunable parameter of O(10^{-4}), q_s and q_{sb} the saturation specific humidity at the parcel level and at cloud base, respectively, and F_0 and F_1 dimensionless vertical scaling functions decreasing strongly with height. Eq. (8) indicates that a drier environment (lower RH) increases the entrainment, suppressing the convection.

Similarly to that in the SC scheme, the entrainment rate in sub-cloud layers is given as inversely proportional to height but with a smaller coefficient of c_e =0.1 in Eq. (6). The detrainment rate is assumed to be a constant in all layers and equal to the entrainment rate value at cloud base, which is O(10^{-4}). The liquid water in the updraft layer is assumed to be detrained from the layers above the level of the minimum moist static energy into the grid-scale cloud water with conversion parameter of 0.002 m^{-1}, which is same as the rain conversion parameter.

c) Momentum transport, trigger function, and convective overshooting

The effect of the convection-induced pressure gradient force on cumulus momentum transport (Han and Pan, 2006) is included in both deep and shallow convection parameterization. Note that momentum transport is absent in the operational SC scheme. A cloud model to describe respectively momentum within the updraft and momentum feedback to the environment can be expressed as

$$\frac{\partial V}{\partial z} = \varepsilon(\overline{V} - V) + f_1 \frac{\partial \overline{V}}{\partial z} \tag{9}$$

$$\frac{\partial \overline{V}}{\partial t} = (1 - f_1) M \frac{1}{\rho} \frac{\partial \overline{V}}{\partial z} + \delta(V - \overline{V}) \tag{10}$$

where V is the horizontal wind vector, M the updraft mass flux, and f_1 an empirical constant representing the effect of the convection-induced pressure gradient force that weakens the cumulus momentum exchange. In the operational SAS scheme, f_1 is zero, implying a full momentum exchange in cumulus convection. In this study, f_1 is set to be 0.55 for both deep and shallow convection schemes, implying that the cumulus momentum exchange is reduced by about 55 % compared to the full exchange.

The trigger condition in the operational SAS scheme is that a parcel lifted from the CSL without entrainment must reach its LFC within 150 hPa of ascent, which crudely represents an upper limit of convective inhibition. The fixed value of 150 hPa is now slightly modified as varying in the range 120-180 hPa, proportional to the large-scale vertical velocity. This modification is intended to produce more convection in large-scale convergent regions but less convection in large-scale subsidence regions. Another important trigger mechanism is to include the effect of environmental humidity in the

sub-cloud layer. Since the scheme allows entrainment in the sub-cloud layers, the LFC becomes higher if drier environmental air entrains into the parcel. In the operational trigger, the vertical model layer difference between the LFCs with and without sub-cloud layer entrainment must be less than two, taking into account convection inhibition due to existence of dry layers below cloud base. This may become a serious deficiency as vertical model resolution changes. In other words, higher (lower) vertical model resolution might give rise to less (more) convection triggering. In the revision, therefore, we use pressure difference instead of model layer difference for the LFC difference. The threshold value for the pressure difference triggering convection is set to be 25 hPa in both deep and shallow convection schemes.

The cloud parcel might overshoot beyond the level of neutral buoyancy due to its inertia, eventually stopping its overshoot at cloud top (Stull, 1988). The cloud work function (CWF, defined as work done by buoyancy force in a cloud; Arakawa and Schubert, 1974) can be used to model the overshoot. In this study, the overshoot of the cloud top is stopped at the height where a parcel lifted from the neutral buoyancy level with energy equal to 10% of the CWF would first have zero energy. This convective overshoot is applied to both deep and shallow convection schemes.

2.2 Vertical diffusion

Readers are urged to refer to Troen and Mahrt (1986; hereafter TM) and Hong and Pan (1996) for detailed description of the MRF PBL model. Here we present only that part relevant to the MRF PBL scheme. As mentioned in the introduction, a cloud-top driven vertical diffusion scheme is incorporated into the MRF PBL model to increase

vertical diffusion in the cloudy region of the lower troposphere, simplified after Lock et al. (2000). In the revised model, the vertical flux for heat is given by

$$\overline{w'\theta'} = -\left(K_h^{surf} + K_h^{Sc}\right)\frac{\partial\overline{\theta}}{\partial z} + K_h^{surf}\gamma_h \qquad (11a)$$

in daytime well-mixed boundary layers, and

$$\overline{w'\theta'} = -\left(K_h(Ri) + K_h^{Sc}\right)\frac{\partial\overline{\theta}}{\partial z} \qquad (11b)$$

in the atmospheric layers above the mixed layer and the nighttime stable boundary layers, where K_h^{surf} and K_h^{Sc} are the surface and cloud top driven eddy diffusivities, respectively, γ_h is the non-local counter-gradient mixing term due to large non-local convective eddies, and $K_h(Ri)$ is the mixing coefficient based on the local Richardson number described later. For the surface-driven diffusion, the vertical diffusivity for momentum, as proposed by TM, is given by

$$K_m^{surf} = \kappa w_s z\left(1-\frac{z}{h}\right)^2 \qquad (12)$$

where κ=*0.4* is the von Karman constant, z the distance from the surface, and h the PBL height. The velocity scale w_s is represented by the value scaled at the top of the surface layer, i.e.,

$$w_s = \left(u_*^3 + 7\alpha\kappa w_*^3\right)^{1/3} \qquad (13)$$

where u_* is the surface friction velocity, α is the ratio of the surface layer height and h specified as 0.1, and w_* is the convective velocity scale defined in Eq. (5). The eddy diffusivity for heat is derived from the K_m^{surf} using the Prandtl number Pr, that is,

K_h^{surf} =Pr^{-1} K_m^{surf}. With the non-local counter-gradient mixing for heat, TM obtain the Prandtl number at the top of the surface layer (z= αh) as

$$\mathrm{Pr} = \frac{\Phi_h}{\Phi_m} + b\alpha\kappa \tag{14}$$

where Φ_h and Φ_m are the non-dimensional gradient functions for heat and momentum, respectively, and b (=6.5) is a coefficient of proportionality. The Prandtl number is assumed constant over the whole PBL.

Following Lock et al. (2000), the stratocumulus top driven diffusivity is given by

$$K_h^{Sc} = 0.85\kappa V_{Sc} \frac{(z - z_b)^2}{h_b - z_b}\left(1 - \frac{z - z_b}{h_b - z_b}\right)^{1/2} \tag{15}$$

where h_b is the level of the stratocumulus top and z_b is the level below cloud base to which the top driven mixing extends. The parameter V_{Sc} represents a cloud top entrainment velocity scale, defined by

$$V_{Sc}^3 = V_{rad}^3 + V_{br}^3 \tag{16}$$

where V_{rad} and V_{br} are radiative cooling and buoyancy reversal terms, respectively. The buoyancy reversal term is neglected in this study. The radiative cooling term is given by

$$V_{rad}^3 = \frac{g}{\theta_0}(h_b - z_b)\Delta R/(\rho c_p) \tag{17}$$

where ΔR is the radiative flux jump at cloud top, ρ the air density, and c_p the specific heat at constant pressure. In order to have an accurate measure of the buoyancy of parcels descending adiabatically from cloud top or ascending adiabatically from the surface, in the revision we use the virtual liquid water potential temperature θ_{vl}[= θ_l(1+0.608q_t), where θ_l= θ-(L/c_p)q_l, q_t=q_v+q_l, q_v and q_l the vapor and liquid water mixing ratio, and L the latent heat of vaporization of water] rather than the virtual potential temperature θ_v. A

parcel descent from the cloud top that determines z_b is made by perturbing the cloud-top θ_{vl} by an amount equal to the cloud-top radiative cooling rate, multiplied by an assumed cloud-top residence timescale of 500 s (Lock et al., 2000). The grid level at which this parcel's θ_{vl} exceeds that of the environment is used to estimate z_b. The presence of stratocumulus is diagnosed by moving a parcel downward from the top of any cloud layer having a liquid water content greater than a threshold value of q_l=3.5×10^{-5}. This diagnosis is restricted to the lowest 2.5 km of the model domain. Then, the cloud top h_b is defined as the level with the largest radiative cooling rate in the cloud layer.

The cloud top entrainment flux is given by

$$-\overline{(w'\theta_v')}_{h_b} = c\frac{\Delta R}{\rho c_p} \tag{18}$$

where c is a constant. In this study, we use c=0.2 following Moeng et al. (1999), implying that 20 % of the total radiative flux jump occurs across the cloud top. When the condition for cloud top entrainment instability (CTEI) is met, however, the stratocumulus top driven diffusion is enhanced by increasing c to 1.0. The condition for the CTEI is given by (Randall,1980; Deardorff, 1980)

$$c_p\Delta\theta_e / L\Delta q_t > c_1 \tag{19}$$

where $\Delta\theta_e$ and Δq_t are the jumps in equivalent potential temperature and total water content across cloud top, and a constant c_1=0.7 (MacVean and Mason, 1990) is used.

For the atmospheric layers above the daytime mixed layer and the nighttime stable boundary layer, we use a local closure scheme (Louis et al., 1982), in which the diffusivity coefficients for momentum and heat are expressed in terms of the mixing

length, l, the stability functions, $f_{m,h}(Ri)$, and the magnitude of the vertical wind shear, $|\partial U / \partial z|$, i.e.,

$$K_{m,h}(Ri) = l^2 f_{m,h}(Ri)\left|\frac{\partial U}{\partial z}\right| \tag{20}$$

In Eq. (20), the mixing length l is given by

$$\frac{1}{l} = \frac{1}{kz} + \frac{1}{l_0} \tag{21}$$

where the asymptotic length scale, l_0, is assumed to be 30m for stable conditions and 150m for unstable conditions. The stability functions, $f_{m,h}(Ri)$, are represented as a function of the local gradient Richardson number, Ri. For stable condition (Ri≥0),

$$f_h(Ri) = \frac{1}{(1+5Ri)^2} \tag{22}$$

with

$$\mathrm{Pr} = 1 + 2.1Ri \tag{23}$$

For unstable conditions (Ri<0),

$$f_h(Ri) = 1 + \frac{8|Ri|}{1+1.286|Ri|^{1/2}} \tag{24}$$

$$f_m(Ri) = 1 + \frac{8|Ri|}{1+1.746|Ri|^{1/2}} \tag{25}$$

The background diffusivity in the current GFS for heat and moisture is exponentially decreased with height from 1.0 m^2s^{-1} as given by

$$K_0 = 1.0e^{\left[-10(1-P/P_s)^2\right]} \tag{26}$$

To avoid too much erosion of stratocumulus along the costal area, the background diffusivity in the lower inversion layers is further reduced to 30% of that at the surface

(i.e., 0.3 m^2s^{-1}). On the other hand, the background diffusivity for momentum has been substantially increased to 3.0 m^2s^{-1} everywhere, which helped reduce the wind forecast errors significantly.

2.3 Cloud fraction

We also modify the present GFS cloud cover calculation because it tends to produce too much low cloud over the entire globe with the new SC scheme. Following Xu and Randall (1996), the fractional cloud cover within grid box (σ) is given by

$$\sigma = RH^{k_1}\left[1-\exp\left(-\frac{k_2 q_l}{\left[(1-RH)q_s\right]^{k_3}}\right)\right] \tag{27}$$

where k_1, k_2 and k_3 are empirical coefficients. Using data produced from explicit simulations of the observed tropical cloud systems, Xu and Randall have obtained the empirical values of k_1, k_2 and k_3, which are 0.25, 100, and 0.49, respectively. In the current GFS model, the values of k_1=0.25, k_2=2000, and k_3=0.25 are used to increase cloud cover because the current SC scheme is too efficient in destroying stratocumulus clouds. Now that the new SC scheme in this study can produce sufficient low clouds, the original empirical values of Xu and Randall (i.e., k_1=0.25, k_2=100, and k_3=0.49) are used.

3. Test and evaluation

3. 1 Coupled model test

To see broad features of the impact of changes in the convection and PBL schemes, we first employ the NCEP atmosphere-ocean coupled forecasting system (CFS; Wang et al., 2005; Saha et al., 2006) where the GFS is used for the atmospheric model.

The GFS used in this test has 64 vertical sigma-pressure hybrid layers and T126 horizontal resolution (about 100 km at equator). The CFS run was initialized at 00Z December 16, 2002 and performed for 45 days. The CFS forecasts during the preceding 15 days (a spin-up period) have been discarded from the analysis, and forecast results during the remaining 1-month period are presented. Evaluation with a longer CFS run would be desirable, but will be left for future study.

Fig. 2a shows that much more realistic low cloud distributions are obtained compared to the control run as the new SC scheme is introduced along with the revised PBL scheme. In particular, improvement for the stratocumulus formation in the regions off the West coasts of the Americas and Africa is remarkable. Without an enhanced diffusion by stratocumulus cloud top driven turbulence, too much low cloud cover is formed, as seen in Fig. 2b. In Fig. 3, we display the distribution of cloud water averaged over latitudes10S to10N to see effect of the SC scheme. With the SC parameterization turned off (Fig. 3b), cloud water is accumulated in lower atmospheric layers just above the PBL, giving rise to unrealistically large low cloud coverage. As shown in Fig. 3a, on the other hand, the operational SC scheme strongly depletes the lower layer cloud water and diffuses it up to the upper layers, forming significant cloud water near 750-600 hPa layers. This is why stratocumulus clouds are lacking with the operational SC scheme. The new SC scheme (Fig. 3c) shows a cloud water distribution intermediate between that with no SC and that with the operational SC scheme, yielding a large improvement in low cloud coverage.

Fig. 4 displays zonally-averaged heating rates due to the SC. The operational SC scheme (Fig. 4a) produces cooling at 700-850 hPa and heating below, showing the

strongest cooling and heating over the tropical regions. This is a typical feature when a parabolic diffusivity profile is applied to stable layers. The upper limit of the cooling layers (i.e., about 700 hPa) is associated with the fact that the shallow cloud top in the operational SC scheme is limited to sigma level 0.7. For the new SC scheme (Fig. 4b), however, the entire lower atmosphere is heated, especially over the tropical and sub-tropical areas (where most of SC occurs) by the dominant environmental subsidence warming typical of convection schemes using the mass-flux approach. Fig. 5 displays a global distribution for monthly mean depth of cumulus clouds. Considering the threshold cloud depth of 150 hPa as distinguishing deep and shallow convection, most of the shallow convection occurs in trade wind areas of the Pacific Ocean and in regions farther out to sea from the stratocumulus regions off the West coasts of America and Africa, consistent with observations.

3. 2 Medium-range forecasts with data assimilation

To assess the impact of the new schemes on forecast skill, 7-day forecasts for the period of June 2 – November 10, 2008 with the NCEP global data assimilation system (GDAS) were conducted. The GFS used in this test has 64 vertical sigma-pressure hybrid layers and T382 horizontal resolution, the same as the current operational version. A spin-up series of forecasts for the previous 19 days has been discarded from the analysis. The results from the operational GFS are presented as the control.

A comparison of anomaly correlations and root-mean-square errors (RMSE) for 500 hPa height as a function of forecast length for both northern (20N-80N) and southern (20S-80S) hemispheres is shown in Fig. 6 and 7, respectively. In the northern

hemisphere, the mean anomaly correlations are significantly higher throughout 7 days of the forecast for the revised model. In the southern hemisphere, the correlations are better for the revised model up to day 5 forecast, but they are slightly worse in day 6 and 7 forecasts. Consistent with the higher anomaly correlation scores, the RMSE are lower. The better results in the northern hemisphere appear to reflect improvement in convection schemes in the revised model since the experiments were conducted for the northern hemisphere summer and fall.

The RMSE for the tropical (20S-20N) 850 and 200 hPa vector winds is shown in Fig. 8. For the 850 hPa vector wind, the RMSE is substantially reduced throughout 7 days of the forecast with the revised model. At 200 hPa, the score with the revised model is also generally improved except for day 1 and 2 forecasts. Figs. 9 and 10 show that the vector wind RMSE for both the northern and southern hemispheres is also significantly reduced with the revised model.

Comparisons of precipitation forecast threat and bias scores over the continental United States are shown in Fig. 11 and 12, respectively. The equitable threat scores (Gandin and Murphy, 1992) with the revised model are better at higher thresholds, while they are slightly worse in very light rain (threshold of 0.2 mm/day) especially for the 12-36 and 36-60 hours forecasts (Fig. 11a and b). The lower score in light rain appears to be associated with the wet bias seen in Fig. 12. Other than in very light rain, the revised model is drier than the control. The drier but better bias score (closer to 1.0) at very high thresholds could be related to the reduction of excessive heavy precipitation - so called 'grid-point storms' which have been a long-standing GFS problem during the convective season. As mentioned in section 2.1b, this could be because the convective

parameterization was not fully eliminating the instability. Fig. 13 shows an example of how the revised model (Fig. 13c) reduces the unrealistic amounts seen in southern Alabama in the control forecasts (Fig. 13b). Fig.14 shows that this unrealistic grid-point storm is mainly from grid-scale precipitation. Larger cloud-base mass flux [Eq. (22)] and higher cloud top in the revised deep convection scheme may have made the major contributions to the reduction of the grid-point storms.

The performance of the revised model against the operational GFS for hurricane forecasts is shown in Fig. 15 and 16 in terms of hurricane track and intensity errors, respectively. As shown in Fig. 15, hurricane track forecasts have been considerably improved with the revised model for both 2008 Atlantic and East Pacific hurricanes. This improvement may be a direct consequence of the improvement in wind forecasts described above. In particular, hurricane intensity forecasts (Fig. 16) have been significantly improved with the revised model especially for the East Pacific hurricanes. The improvement in the hurricane intensity forecasts is mainly due to the reduced momentum mixing in the revised deep and shallow convection schemes accomplished by taking into account the convection-induced pressure gradient force, as studied in Han and Pan (2006).

4. Summary and conclusions

The new physics package containing the revised convection and PBL schemes and its impact on the NCEP GFS has been described. The new SC scheme employs a mass flux parameterization, which may be more physically appropriate than the operational scheme (a turbulent diffusion scheme). Unlike the deep convection scheme,

mass flux at cloud base in the new SC scheme is given as a function of the convective boundary layer velocity scale. For the deep convection scheme, random cloud top selection in the current SAS scheme is replaced by an entrainment rate approach with the rate dependent on environmental moisture. The effects of the convection-induced pressure gradient force on cumulus momentum transport and convective overshooting are parameterized in both the deep and shallow convection schemes and a modification of the trigger function has been developed. In addition, the PBL model is revised to enhance turbulence diffusion in stratocumulus regions.

A remarkable difference between the new and operational SC schemes is seen in heating or cooling behavior in lower atmospheric layers above the PBL. While the operational SC scheme using the diffusion approach produces a pair of layers with cooling above and heating below in lower atmospheric layers, the new SC scheme using the mass-flux approach produces heating throughout the convection layers due to the dominant environmental subsidence warming. In particular, the new SC scheme helps to form stratocumulus clouds in the regions off the West coasts of South America and Africa, whereas the old scheme destroys them.

The revised model improves the model forecast skill overall. Significant improvements in the forecasts of the global 500 hPa height, vector wind, and precipitation over the continental US are found with the revised model. In particular, unrealistic forecasts of excessive heavy precipitation have been reduced probably due to larger cloud base mass flux and higher cloud top in the revised deep convection scheme, which appears to help eliminate the instability. Along with improvement in vector wind forecast errors, hurricane track forecasts are considerably improved with the revised

model for both 2008 Atlantic and East Pacific hurricanes. In particular, hurricane intensity forecast biases are greatly reduced mainly due to the reduced momentum mixing by the convection-induced pressure gradient force.

The revised model presented in this paper has been implemented operationally in the NCEP GFS as of late July, 2010. For future revisions, convective cloudiness and advanced moist turbulence parameterization are under development. Contribution to cloudiness by the cumulus convection in the current revised model is indirectly taken into account by the detrainment of the liquid water from the convective updrafts into the grid-scale cloud water. A direct convective cloudiness can be included by considering the suspended liquid water in the convective updraft. The current revised diffusion scheme has an enhanced turbulence mixing in the stratocumulus region. But, it is still based on variables conserved in dry adiabatic processes and thus, may not be appropriate for treating cloudy layer mixing, which needs consideration of the latent heating associated with changes of state of water. In further revisions, the model's turbulence mixing will be expressed in terms of variables conserved during changes of state of water, allowing more realistic calculation of atmospheric stability and moist turbulence mixing in cloudy regions.

Acknowledgments

The authors highly appreciate help and many suggestions from S. Moorthi (for the GFS run), Suranjana Saha (for the CFS run), Russ Treadon (for using GSI data assimilation system), and Fanglin Yang (for running the GFS forecasts with data assimilation and computing GFS forecast skill scores) at NCEP/EMC. Internal reviews

from Peter Caplan, Fanglin Yang, and Masayuki Nakagawa at NCEP/EMC are acknowledged. We are also grateful to John Ward and Steve Lord at NCEP/EMC for their encouragements on this work.

References

Arakawa, A., and W. H. Schubert, 1974: Interaction of a cumulus cloud ensemble with the large-scale environment, Part I. *J. Atmos. Sci.*, **31**, 674-701.

Bechtold, P., M. Kohler, T. Jung, F. Doblas-Reyes, M. Leutbecher, M. J. Rodwell, F. Vitart, and G. Balsamo, 2008: Advances in simulating atmospheric variability with the ECMWF model: From synoptic to decadal time-scales. *Quart. J. Roy. Meteor.* Soc., **134**, 1337-1351.

Caplan, P., J. Derber, W. Gemmill, S.-Y. Hong, H.-L. Pan, and D. Parrish, 1997: Changes to the 1995 NCEP operational medium-range forecast model analysis-forecast system. *Wea. and Forecasting,* 12, 581-594.

Deardorff, J. W., 1980: Cloud-top entrainment instability. *J. Atmos. Sci.,* 37, 131-147.

de Roode, S. R., P. G. Duynkerke, and A. P. Siebesma, 2000: Analogies between Mass-Flux and Reynolds-Averaged Equations. *J. Atmos. Sci.,* 57, 1585-1598.

Gandin, L. S., and A. H. Murphy, 1992: Equitable skill scores for categorical forecasts. *Mon. Wea. Rev.,* **120**, 361-370.

Grant, A. L. M., 2001: Cloud-base fluxes in the cumulus-capped boundary layer. *Quart. J. Roy. Meteor.* Soc., **127**, 407-422.

Grant, A. L. M., and A. R. Brown, 1999: A similarity hypothesis for shallow cumulus transports. *Quart. J. Roy. Meteor.* Soc., **125**, 1913-1936.

Han, J., and H.-L. Pan, 2006: Sensitivity of hurricane intensity forecast to convective momentum transport parameterization. *Mon. Wea. Rev.*, **134**, 664-674.

Hong S.-Y., and H.-L. Pan, 1996: Nonlocal boundary layer vertical diffusion in a Medium-Range Forecast model. *Mon. Wea. Rev.*, **124**, 2322–2339.

Jakob, C., and A. P. Siebesman, 2003: A new subcloud model for mass-flux convection schemes: Influence on triggering, updraft properties, and model climate. *Mon. Wea. Rev*, **131**, 2765–2778.

Lock, A. P., A. R. Brown, M. R. Bush, G. M. Martin, and R. N. B. Smith, 2000: A new boundary layer mixing scheme. Part I: Scheme description and single column model tests. *Mon. Wea. Rev.,* 128, 3187–3199.

Louis, J. F., M. Tiedtke, and J. F. Geleyn, 1982: 'A short history of the PBL parameterization at ECMWF'. Pp 59-79 in Proceedings of Workshop on boundary-layer parameterization. ECMWF, Reading, UK.

MacVean, M. K. and P. J. Mason, 1990: Cloud-top entrainment instability through small-scale mixing and its parameterization in numerical models. *J. Atmos. Sci.,* 47, 1012-1030.

Moeng, C.-H., P. P. Sullivan, and B. Stevens, 1999: Including radiative effects in an entrainment-rate formula for buoyancy driven PBLs. *J. Atmos. Sci.,* 56, 1031–1049.

Pan, H.-L., and W.-S. Wu, 1995: Implementing a mass flux convective parameterization package for the NMC medium-range forecast model. NMC Office Note 409, 40 pp.

Raga, G. B., J. B. Jensen, and M. B. Baker, 1990: Charateristics of cumulus band clouds off the coast of Hawaii. *J. Atmos. Sci.*, **47**, 338-355.

Randall, D. A., 1980: Conditional instability of the first kind upside-down. *J. Atmos. Sci.,* 37, 125-130.

Rossow, W.B., and R. A. Schiffer, 1991: ISCCP Cloud Data Products. *Bull. Amer. Meteor. Soc.*, **71**, 2-20.

Saha, S., S. Nadiga, C. Thiaw, J. Wang, W. Wang, Q. Zhang, H. M. Van den Dool, H.-L. Pan, S. Moorthi, D. Behringer, D. Stokes, M. Peña, S. Lord, G. White, W.
Siebesma, A. P., and J. W. M. Cuijpers, 1995: Evaluation of parametric assumptions for shallow cumulus convection. *J. Atmos. Sci.*, **52**, 650-666.

Siebesma, A. P., C. S. Bretherton, A. Brown, A. Chlond, J. Cuxart, P. G. Duynkerke, H. L. Jiang, D. Lewellen, C. H. Moeng, E. Sanchez, B. Stevens, and D. E. Stevens, 2003: A large eddy simulation intercomparison study of shallow cumulus convection. *J. Atmos. Sci.*, **60**, 1201-1219.

Stull, R. B., 1988: An introduction to boundary layer meteorology. *Kluwer Academic Publishers*, 666 pp.

Tiedtke, M., W. A. Heckley, and J. Slingo, 1988: Tropical forecasting at ECMWF: The influence of physical parameterization on the mean structure of forecasts and analyses. *Quart. J. Roy. Meteor.* Soc., **114**, 639-644.

Troen I., and L. Mahrt, 1986: A simple model of the atmospheric boundary layer sensitivity to surface evaporation. *Bound.-Layer Meteor.*, **37**, 129–148.

Wang, W., S. Saha, H.-L. Pan, S. Nadiga, and G. White, 2005: Simulation of ENSO in the new NCEP coupled forecast system model (CFS03). *Mon. Wea. Rev.,* 133, 1574–1593.

Xu, K.-M., and D. A. Randall, 1996: A semiempirical cloudiness parameterization for use in climate models. *J. Atmos. Sci.*, **53**, 3084-3102.

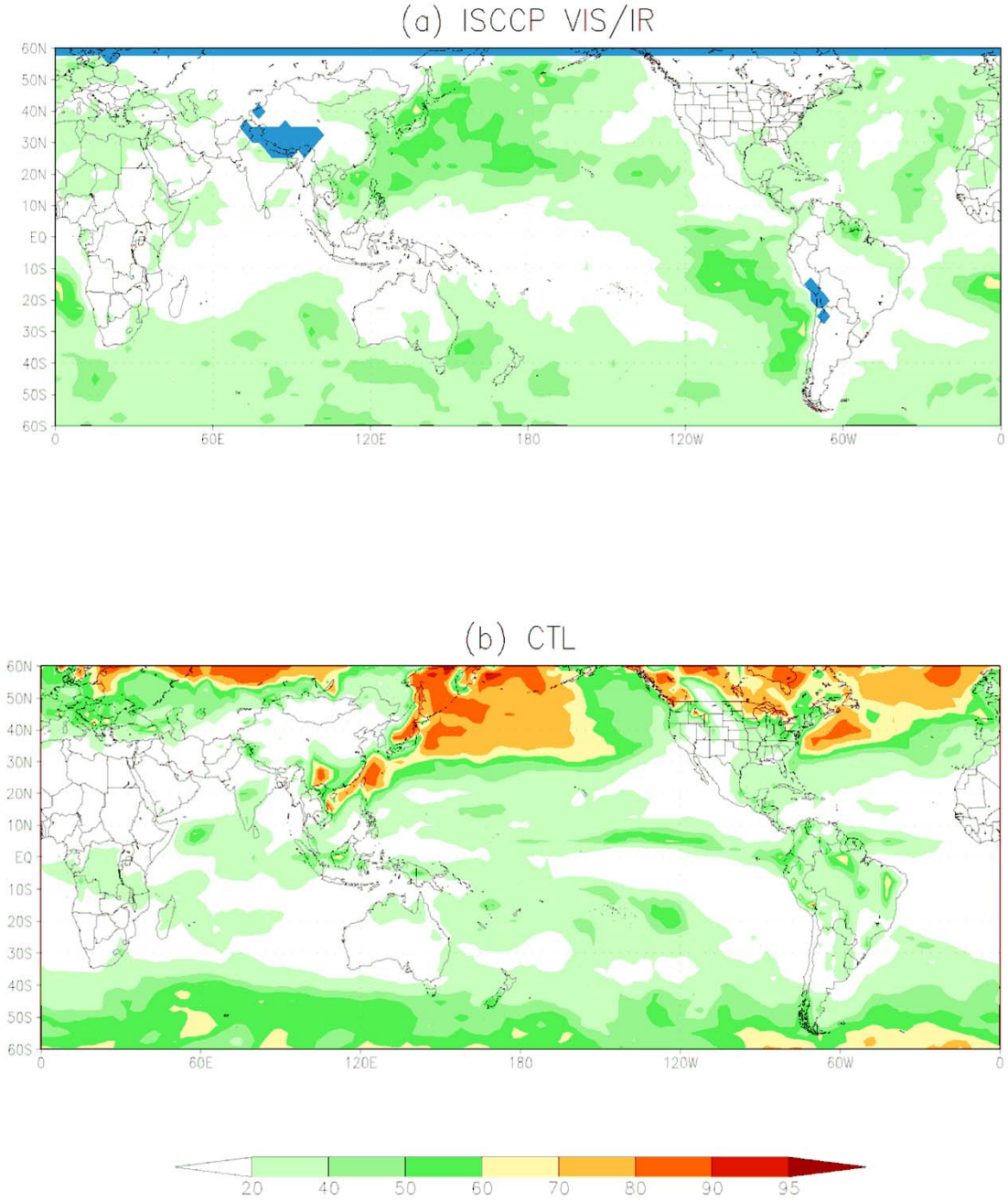

Fig. 1. Monthly mean low cloud cover (%) for January 2003 from (a) ISCCP (International Satellite Cloud Climatology Project; Rossow and Schiffer, 1991) VIS/IR satellite observations (regions with no data available are shown as blue color) and (b) control simulation.

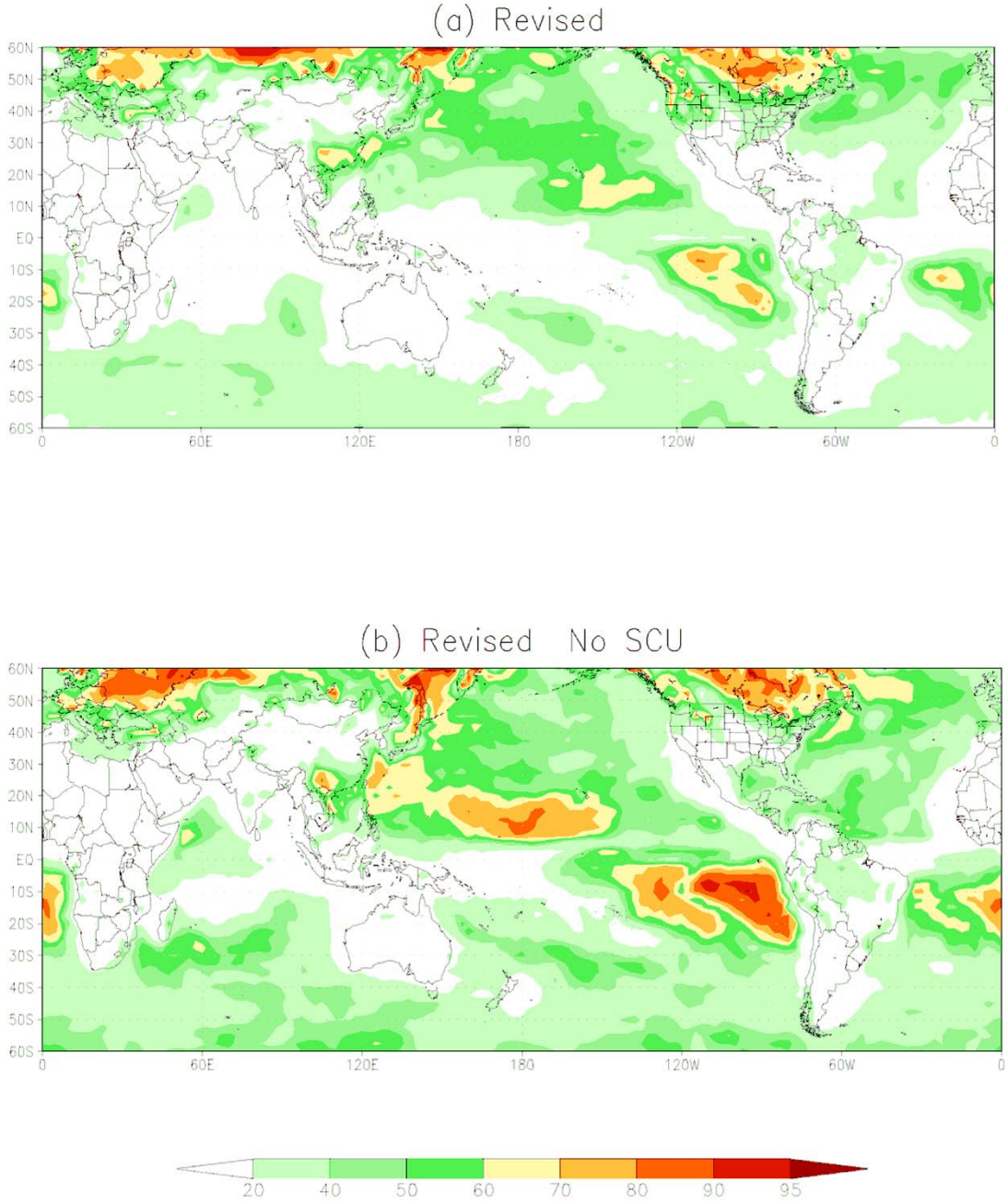

Fig. 2. Same as Fig. 1 but from (a) revised model simulation and (b) revised model simulation without stratocumulus cloud top driven turbulence mixing.

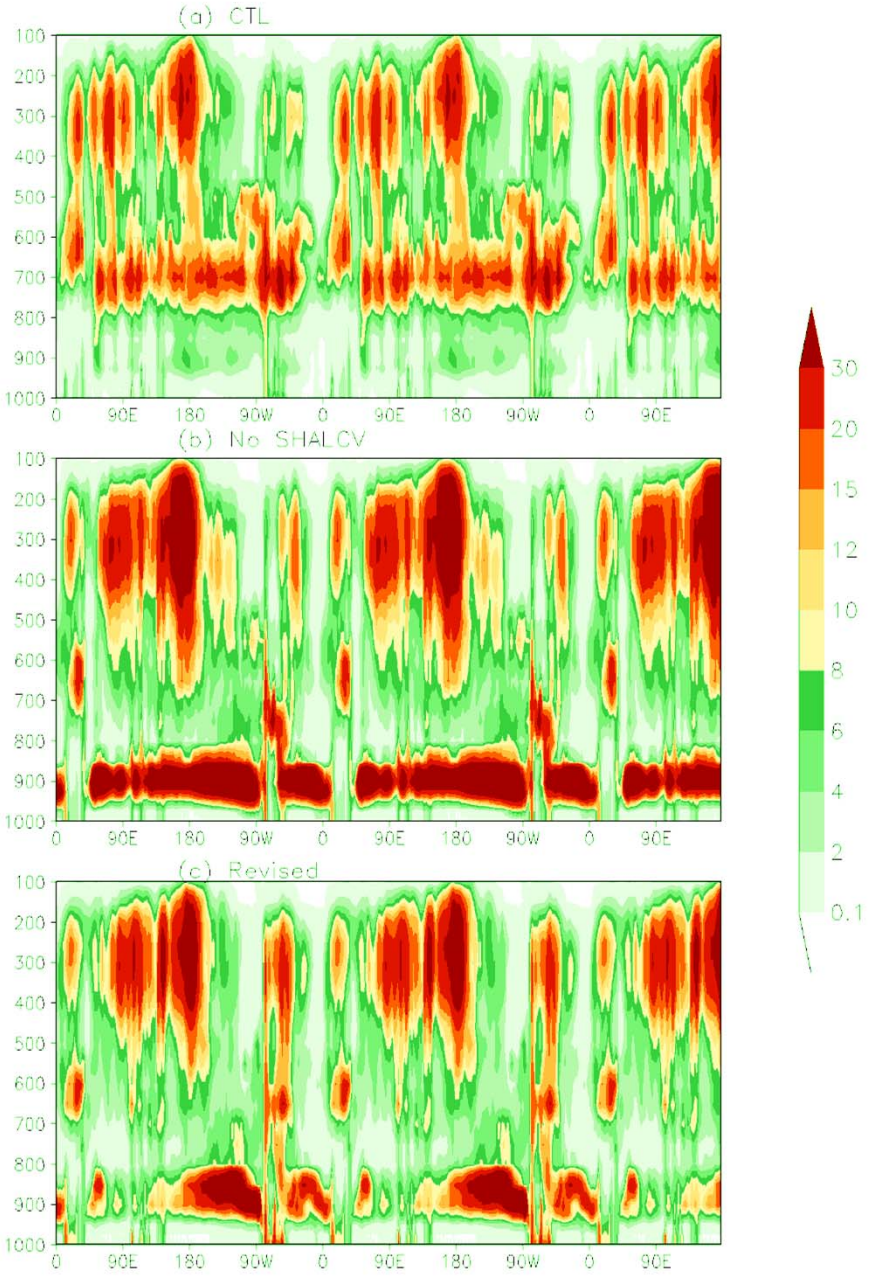

Fig. 3. Vertical cross section of mean cloud water (mg/kg) averaged over latitudes 10S to10N for January 2003 from (a) control simulation, (b) control simulation without triggering shallow convection, and (c) revised model simulation.

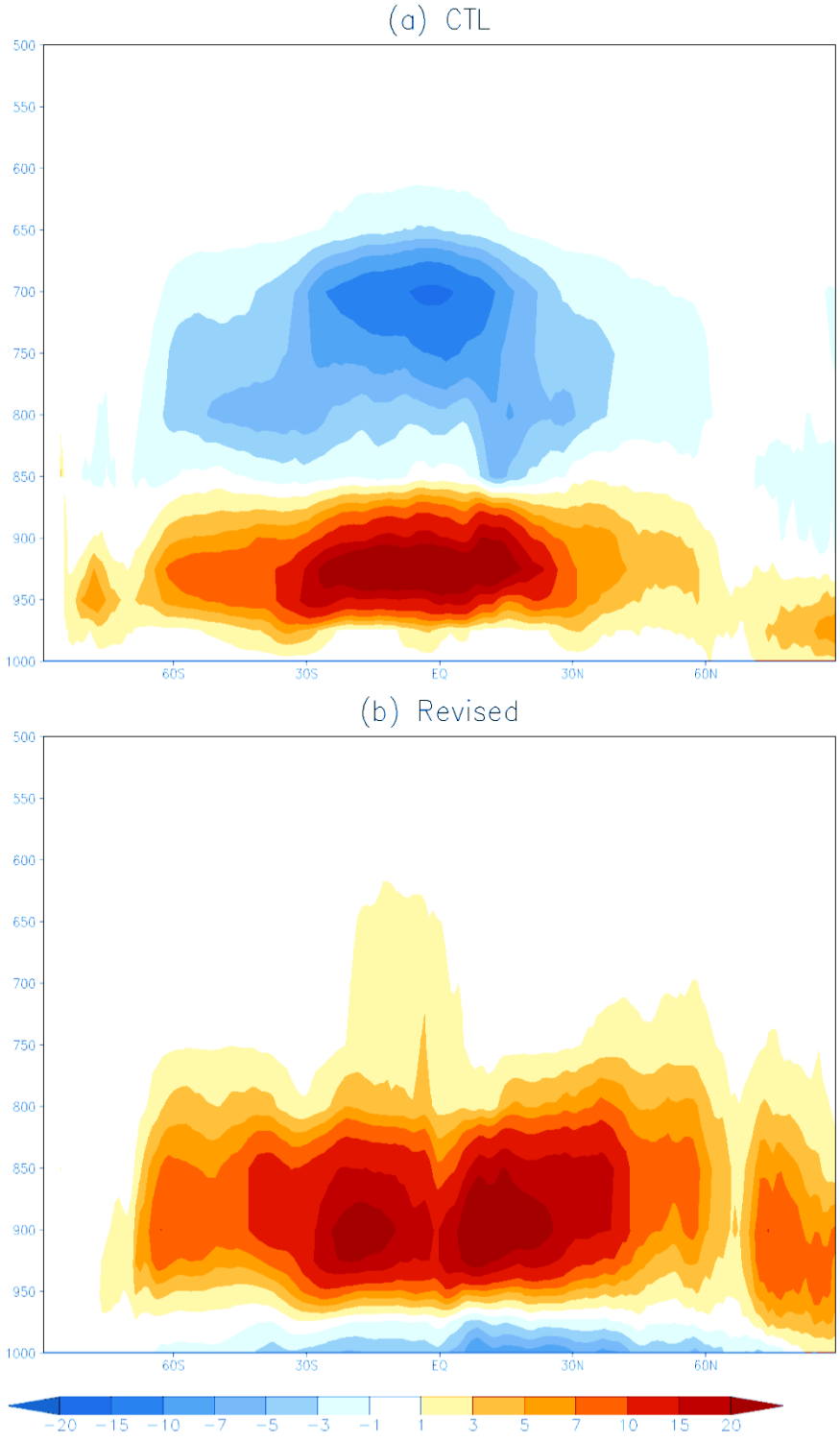

Fig. 4. Zonally averaged heating rates (10^{-6} K/s) due to the shallow convection for January 2003 from (a) control simulation and (b) revised model simulation.

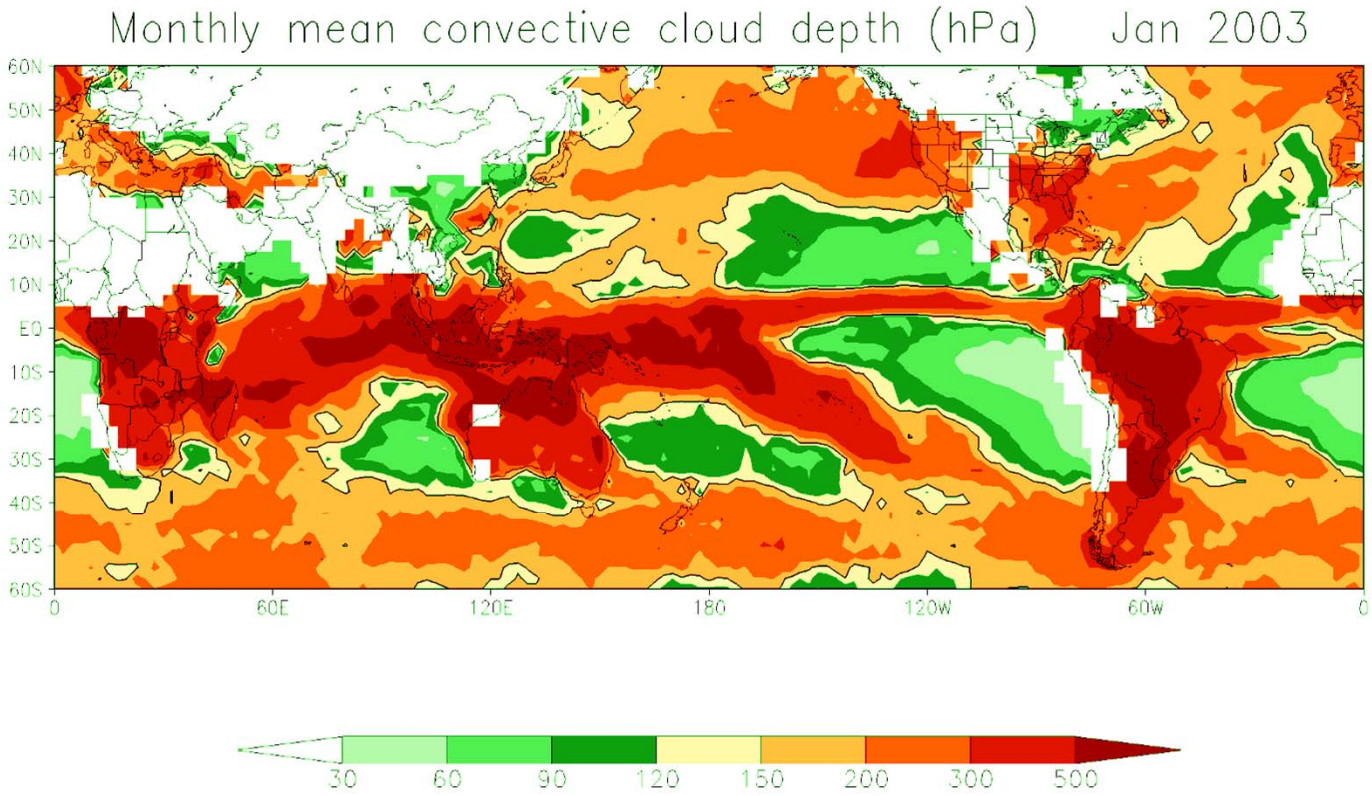

Fig. 5. Monthly mean convective cloud depth (hPa) from the revised model simulation. The thick solid contour indicates the cloud depth of 150 hPa.

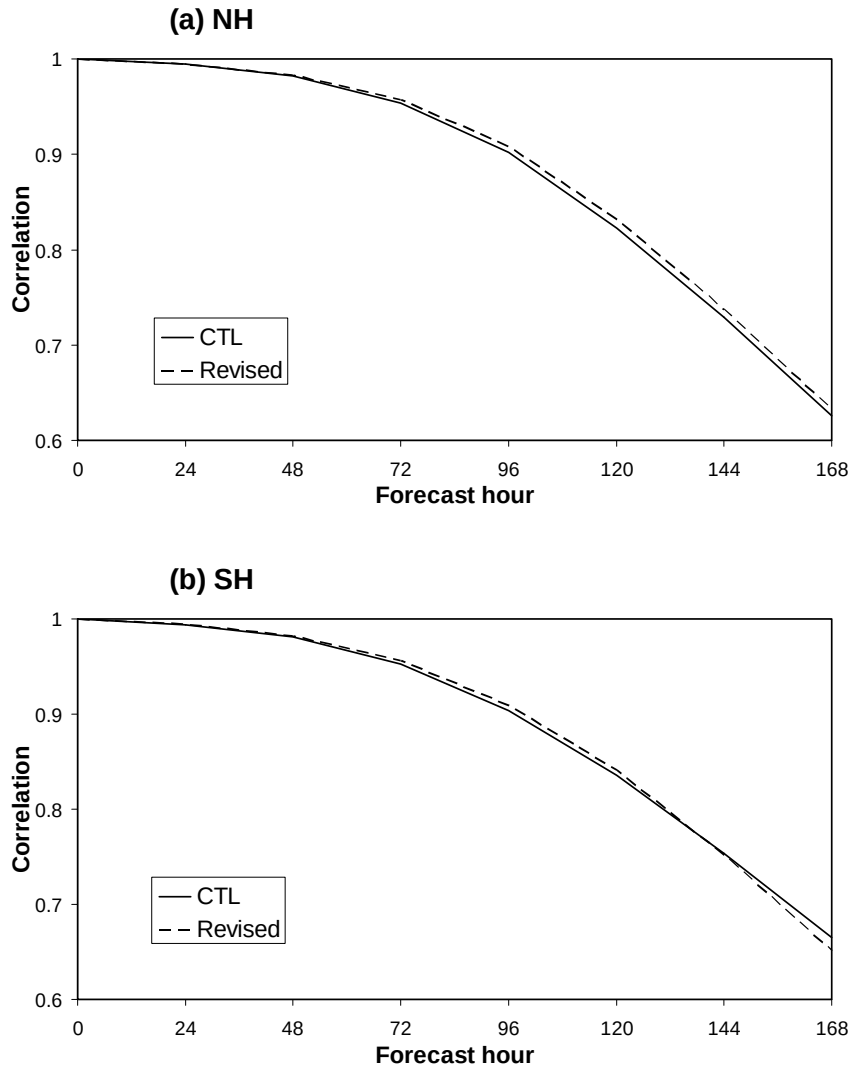

Fig. 6. Mean anomaly correlations of 500 hPa heights for (a) Northern Hemisphere (20N-80N) and (b) Southern Hemisphere (20S-80S) from the control and revised model forecasts verifying June 20 – November 10, 2008 as a function of forecast length.

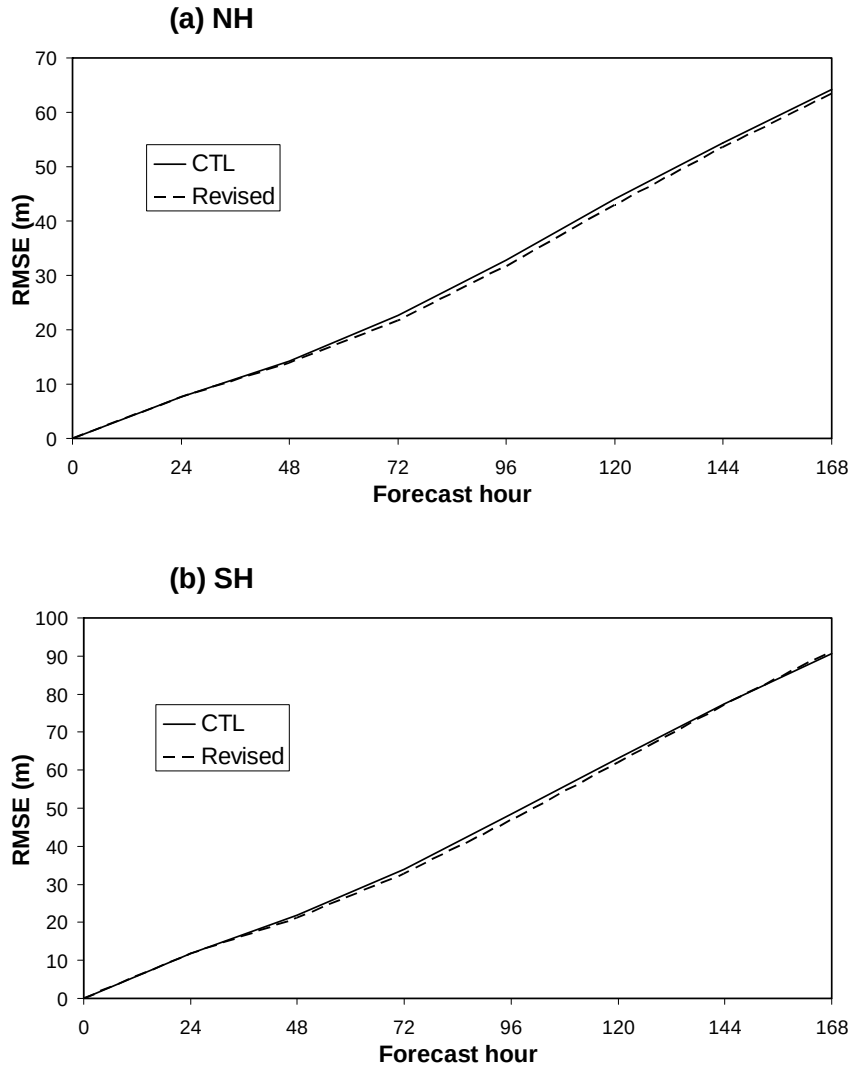

Fig. 7. Same as Fig. 6 but for root mean square error (m).

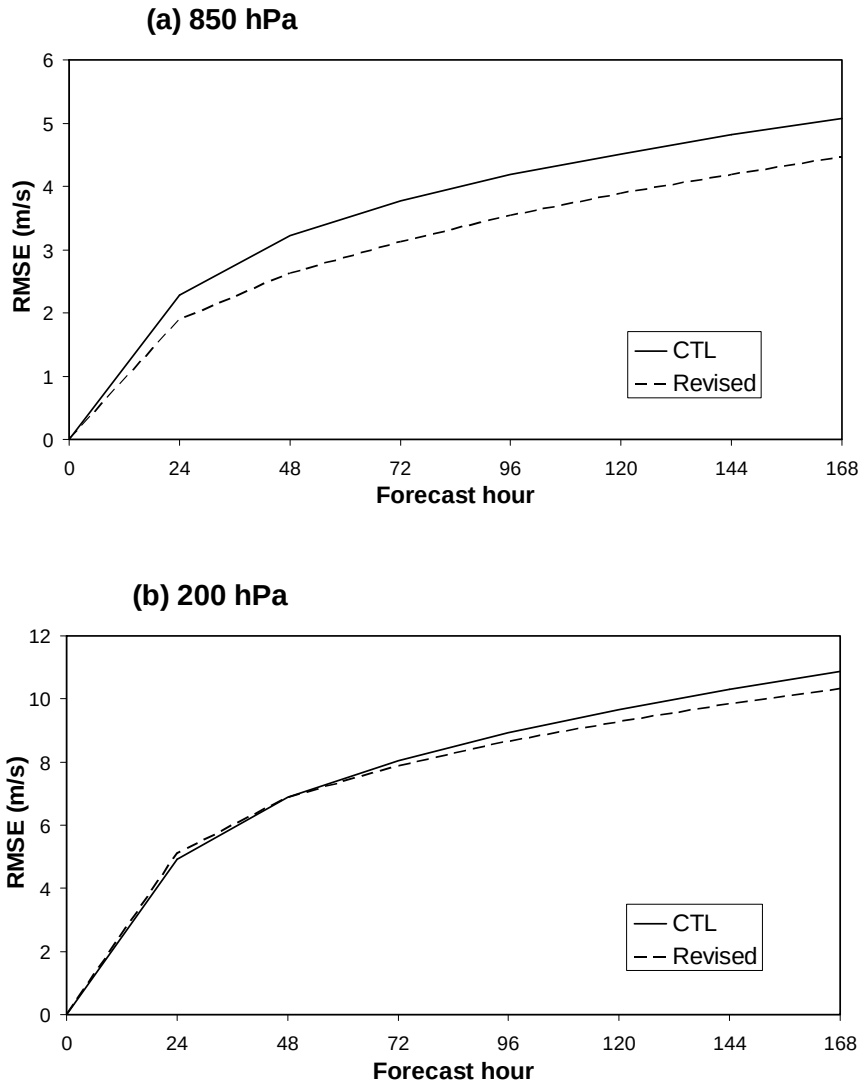

Fig. 8. Same as Fig. 6 but for root mean square vector wind error (m/s) at (a) 850 hPa and (b) 200 hPa over the Tropics (20S-20N) .

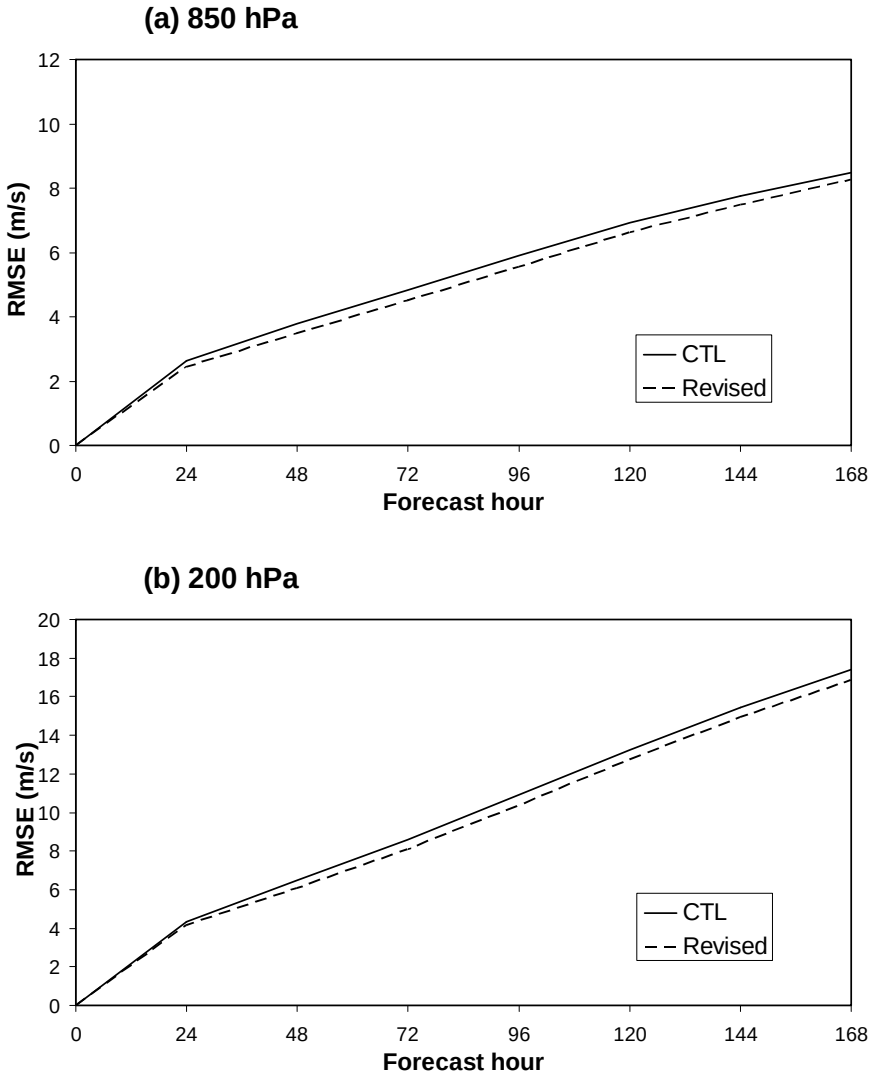

Fig. 9. Same as Fig. 8 but over the Northern Hemisphere (20N-80N).

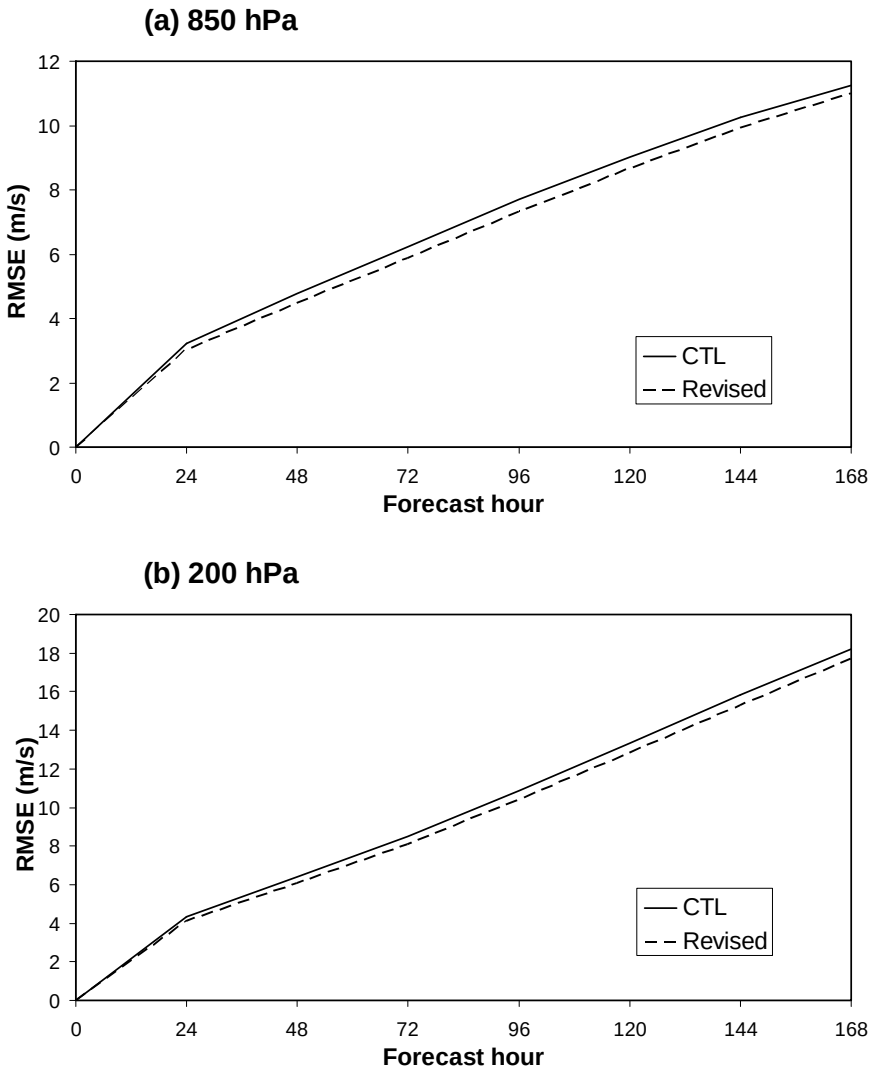

Fig. 10. Same as Fig. 8 but over the Southern Hemisphere (20S-80S).

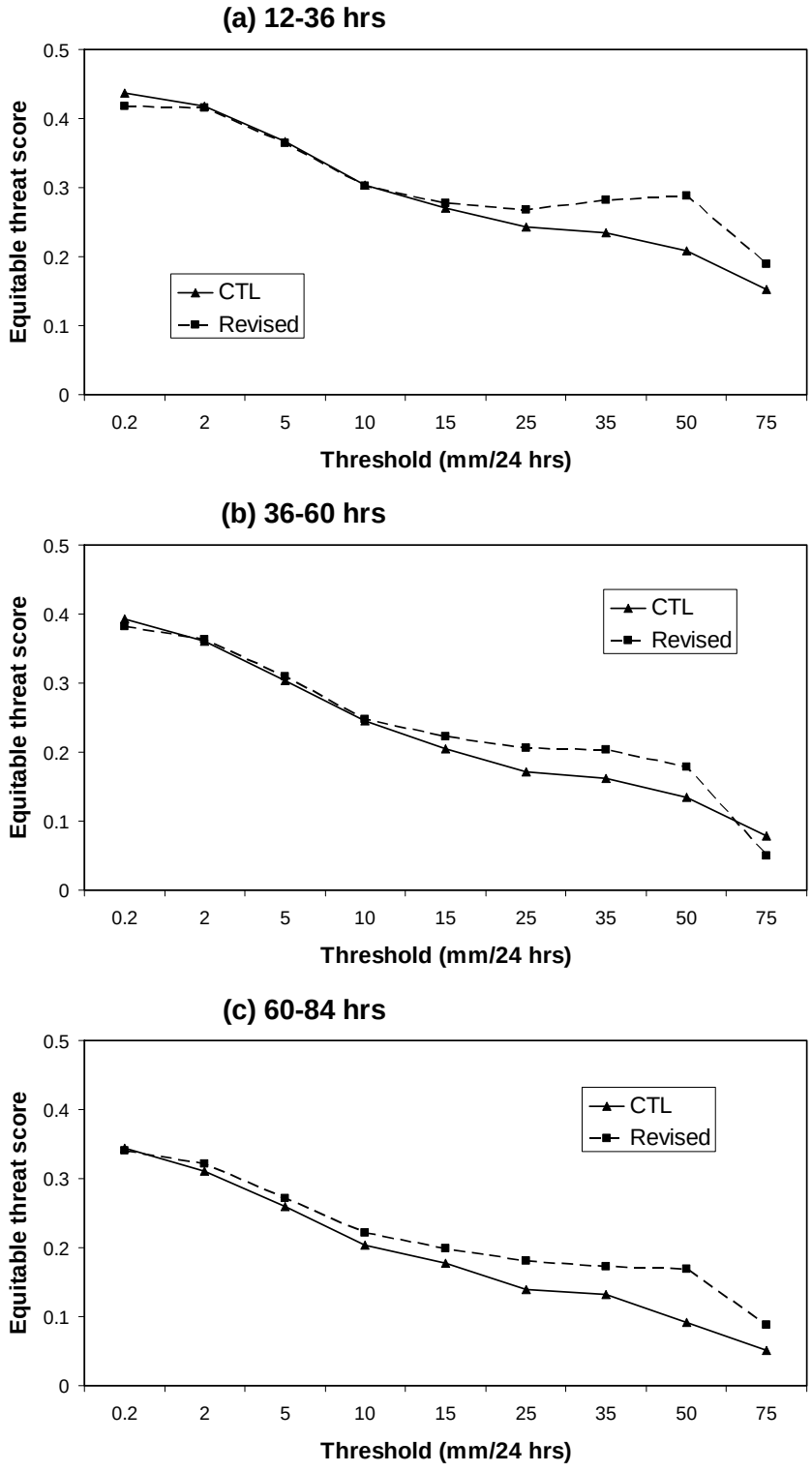

Fig. 11. Same as Fig. 6 but for equitable threat scores for (a) 12-36 h, (b) 36-60 h, and (c) 60-84 h precipitation forecasts over the continental United States.

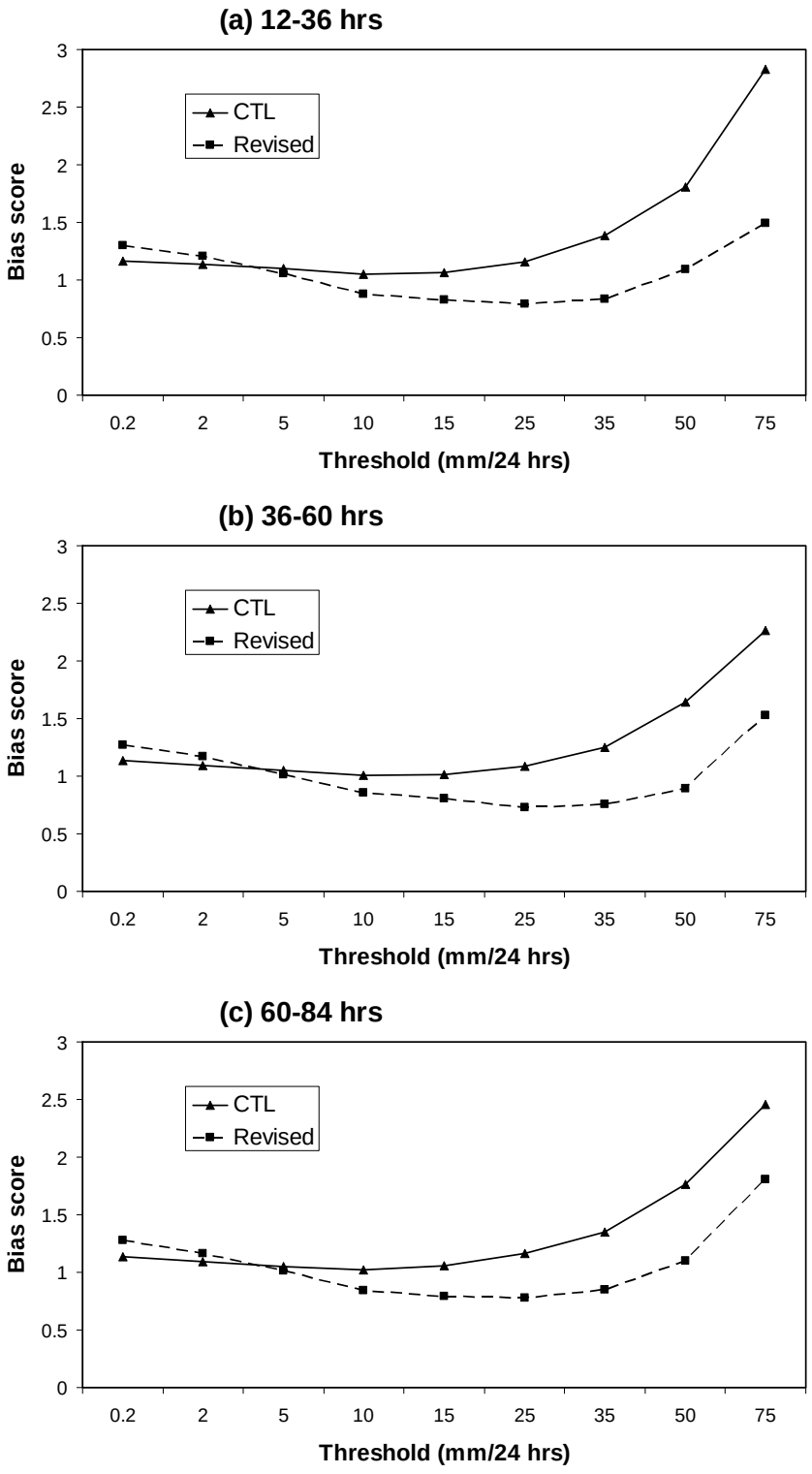

Fig. 12. Same as Fig. 11 but for the precipitation bias scores.

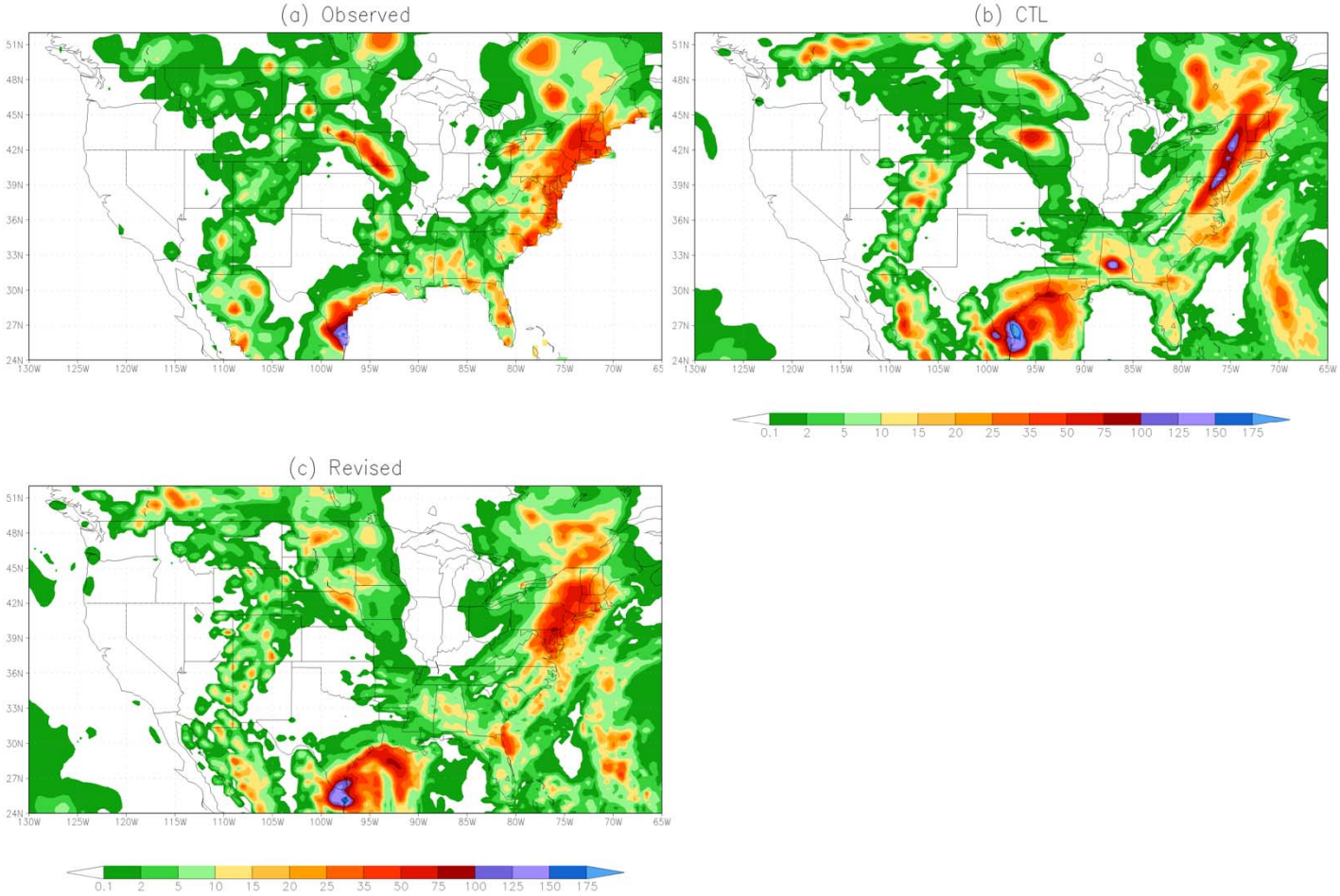

Fig. 13. 24 h accumulated precipitation (mm) ending at 12 UTC, July 24, 2008 from (a) observation and 12-36 h forecasts with (b) control GFS and (c) revised model.

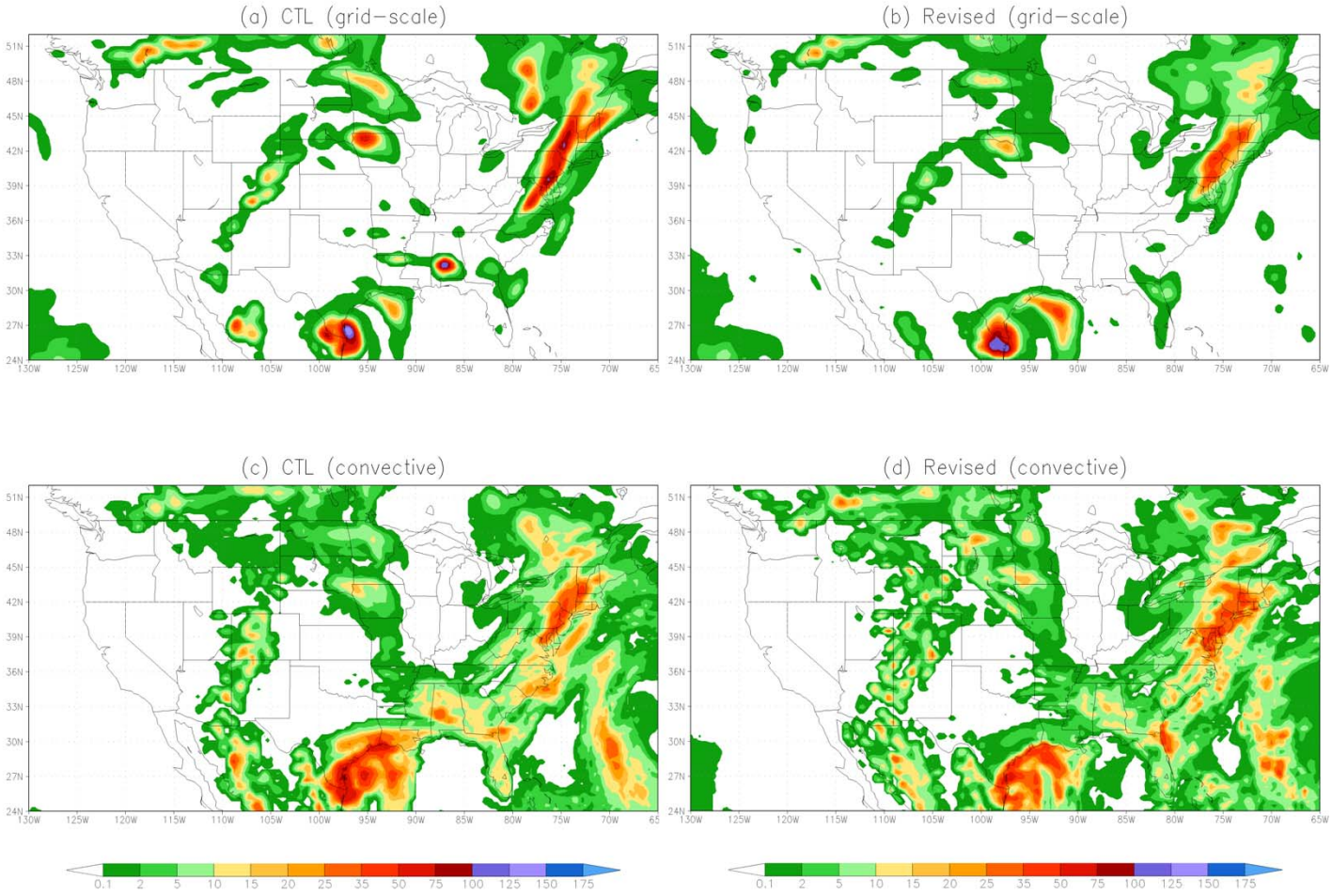

Fig. 14. Same as Fig. 13b,c but for the grid-scale (a, b) and convective (c, d) precipitations, respectively.

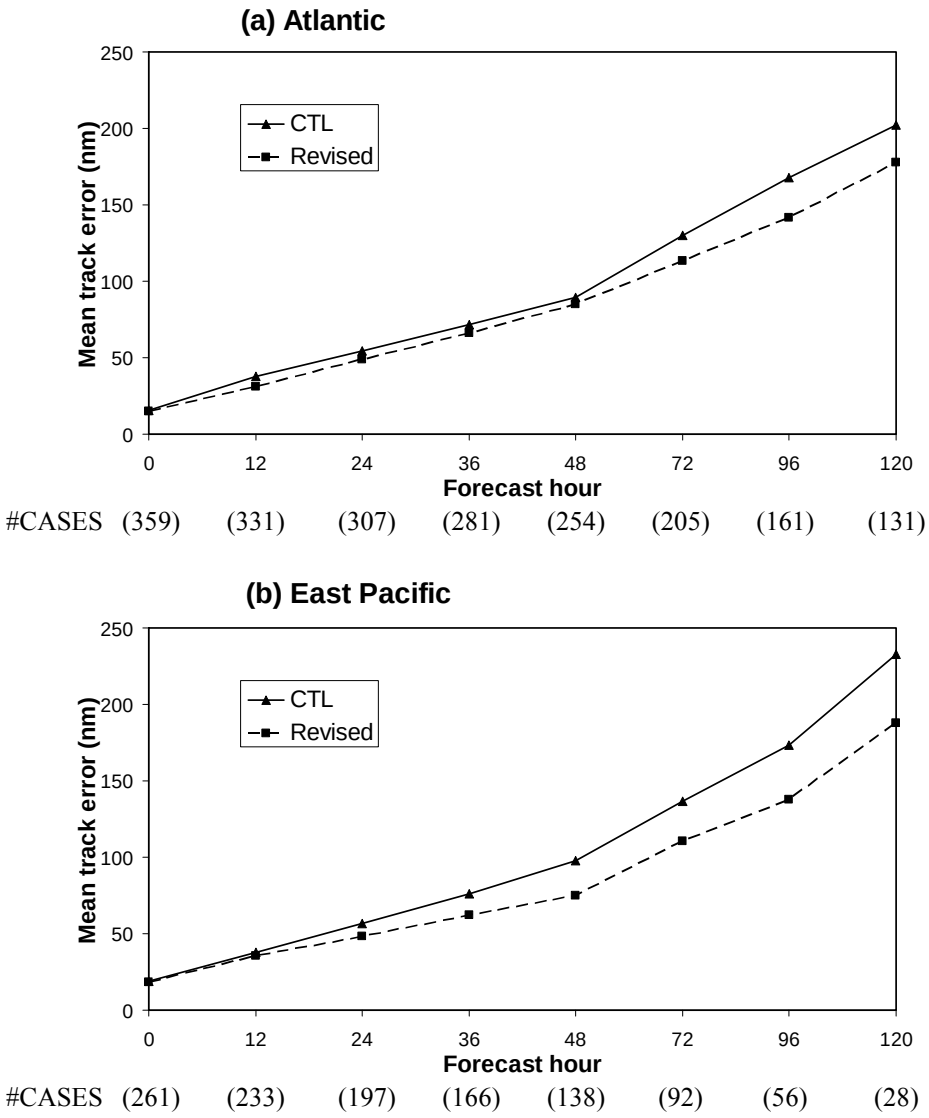

Fig. 15. Mean hurricane track errors for (a) Atlantic Ocean regions and (b) East Pacific Ocean regions, computed from the control and revised model forecasts during June 2 – November 10, 2008.

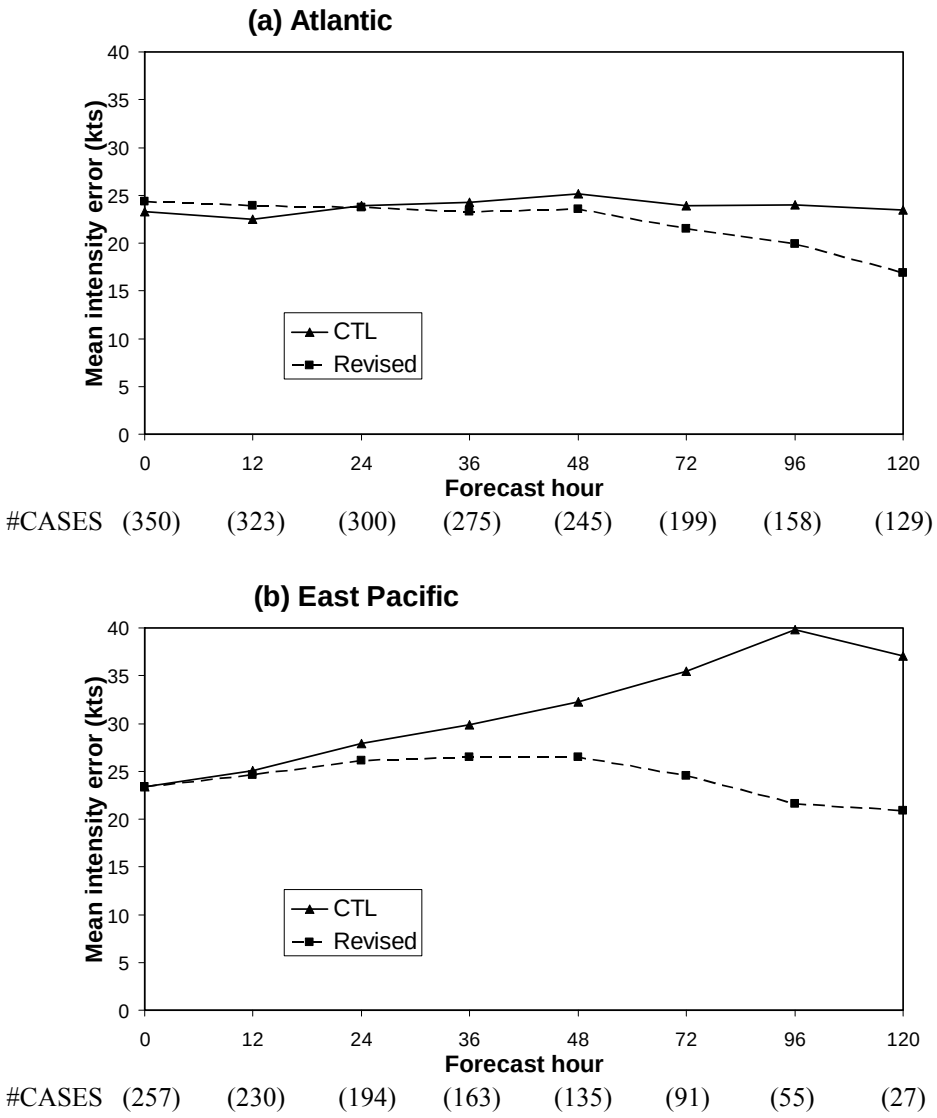

Fig. 16. Same as Fig. 15 but for mean hurricane intensity errors.